In Depth Mapping of Mesoporous Silica Nanoparticles in Malignant Glioma Cells Using Scattering-Type Scanning Near-Field Optical Microscopy

Published as part of Chemical & Biomedical Imaging special issue "Sub-diffraction Chemical Imaging".

George E. Greaves,* Alessandra Pinna, Jonathan M. Taylor, Alexandra E. Porter, and Chris C. Phillips*

Cite This: *Chem. Biomed. Imaging* 2024, 2, 842−849

Read Online

| ACCESS | Metrics & More | Article Recommendations | Supporting Information |

ABSTRACT: Mesoporous silica nanoparticles (MSNPs) are promising nanomedicine vehicles due to their biocompatibility and ability to carry large cargoes. It is critical in nanomedicine development to be able to map their uptake in cells, including distinguishing surface associated MSNPs from those that are embedded or internalized into cells. Conventional nanoscale imaging techniques, such as electron and fluorescence microscopies, however, generally require the use of stains and labels to image both the biological material and the nanomedicines, which can interfere with the biological processes at play. We demonstrate an alternative imaging technique for investigating the interactions between cells and nanostructures, scattering-type scanning near-field optical microscopy (s-SNOM). s-SNOM combines the chemical sensitivity of infrared spectroscopy with the nanoscale spatial resolving power of scanning probe microscopy. We use the technique to chemically map the uptake of MSNPs in whole human glioblastoma cells and show that the simultaneously acquired topographical information can provide the embedding status of the MSNPs. We focus our imaging efforts on the lamellipodia and filopodia structures at the peripheries of the cells due to their significance in cancer invasiveness.

KEYWORDS: *Infrared imaging, subdiffraction, spectroscopy, s-SNOM, nanoparticles, nanomedicine*
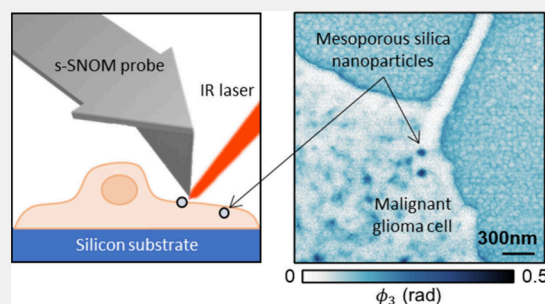
■ INTRODUCTION

Scattering-type scanning near-field optical microscopy (s-SNOM) uses a sharp conducting probe that is illuminated by a light source and brought close enough to a sample to probe its optical near-field. The tip (usually part of an atomic force microscope (AFM)) oscillates vertically, and by analyzing the light that is backscattered from the region where it interacts with the sample, the optical properties of a small sample patch can be measured.

In the commonly employed pseudoheterodyne detection regime,[1] the amplitude and phase of the backscattered light from the sample are independently measured, and, in the case of weak harmonic oscillators such as the vibrational modes probed here, relate to the real and imaginary parts of the dielectric function of the sample, respectively.[2] The imaginary part of the dielectric function exhibits peaks centered around the resonant frequencies of vibrational modes of the chemical groups in the sample. Thus, the phase measurement is proportional to the far-field absorption coefficient of the sample at the wavelength of the illumination.[3]

With a suitable choice of light source, or sources, s-SNOM enables near-field imaging[4] at multiple wavelengths, allowing one to generate nanometre scale chemical maps of samples.[5,6] We use quantum cascade lasers (QCLs), which are tunable throughout the mid-infrared, and are commonly employed in s-SNOM.[7]

The high spatial frequency sample information is contained in the optical near-field, which decays exponentially in magnitude with distance from the sample surface. Bringing a probe close to the sample surface results in the near-field manifesting in the backscattered light from the probe. The extent to which the near-field modifies the backscattered light varies nonlinearly with the height of the probe above the sample. Thus, when the probe is oscillated above the sample, the backscattered light contains frequency components at the harmonics of the oscillation frequency. By analyzing the backscattered light at these harmonics, the near-field component of the backscattered light, and thus the high spatial frequency information, is recovered. The nonlinearity in the backscattered light is related to the radius of curvature of
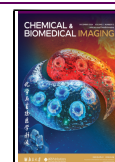
the tip of the probe.[8] Ultimately, therefore, the spatial resolution of s-SNOM is determined by the tip radius (5—50 nm), not the illumination wavelength, and beats the normal diffraction limit by several decades.[9,10]

Imaging of cancer cells is key for understanding processes, such as cell migration and invasiveness. Examples include migration inhibition with the application of flavonoids,[11] and cell—cell transfer of organelles through tunnelling nanotubes.[12] These processes are determined by nanoscale peripheral cell structures such as lamellipodia and filopodia;[11] these are the protrusions involved in cell motility and migration, both of which play critical roles in cancer progression and metastasis.[13]

Infrared spectra acquired from cells represent a unique biochemical fingerprint, providing information about the biomolecules they contain, such as those that comprise the cell's organelles. Previously we have shown that s-SNOM can be used for nanoscale chemical imaging of subcellular organelles and internalized gold nanoparticles within ultrathin (70—200 nm) sections of primary neurons[14] and multiple myeloma cells.[15]

These studies combined the nanoscale resolution of s-SNOM (down to 5 nm[16]) with the chemical sensitivity of IR spectroscopy. We are able to map biochemical fingerprints from intracellular structures and assorted biomolecules as well as nanoparticles that are currently being developed as imaging probes or nanomedicines.

Raman spectroscopy is also used to probe biochemical fingerprints and has been used to diagnose cancer using biomarkers.[17−20] However, the technique suffers from a low scattering cross section which can make it difficult to image and generate chemical maps of unlabeled samples when compared with s-SNOM.[21] Nonetheless, s-SNOM and tip-enhanced Raman spectroscopy (TERS) are complementary techniques and can both be employed as part of multimodal imaging setups.[22]

Imaging of whole cancer cells represents an exciting yet largely unexplored area for s-SNOM. Examples include imaging amyloid β-sheets on the surface of neurons without requiring immunolabeling,[23] as well as imaging the surface of red blood cells.[24] The s-SNOM signal originates from sample depths that are roughly commensurate with the lateral resolution, so images of whole cells have a dominant contribution from the ~10 nm cell membrane and generally only offer information on the surface features. However, it is possible to identify a contribution to the s-SNOM signal from components below the surface in both plane[25,26] and spherical (nanoparticle)[27] geometries.

Here we take a step toward chemically imaging internal structures by first imaging the internal volume of cells.[28] We image through the depth of a glioblastoma multiforme (GBM) cell line, U-87 MG. These are significantly larger (~50−100 μm) than the multiple myeloma cells and hippocampal neurons (~10 μm) investigated in our previous work.[14,15] As demonstration, we study the internalization of mesoporous silica nanoparticles (MSNPs), and we show that constituents of whole cells can be imaged using s-SNOM.

The MSNP example was chosen because their high biocompatibility, degradability, and ease of functionalization and surface modification for specific cell targeting[29] gives them a range of applications in nanomedicine. Compared to dense silica nanoparticles,[30,31] MSNPs offer nanometer size porosity and large pore volume (0.48−1.21 cm³/g) and surface area

(700−1000 m²/g, ca. x30), giving them a correspondingly high drug-loading capacity.[32]

We first present s-SNOM and AFM imaging of the periphery of a U-87 MG cell, studying the three-dimensional cell surface morphology, including lamellipodia and filopodia. Subsequently we use the IR chemical signature of MSNPs to map their distribution in a U-87 MG cell and to determine their locations by combining the chemical and topographical mappings.

■ RESULTS AND DISCUSSION

Mesoporous Silica Nanoparticles (MSNPs)

The protocol used to synthesize the MSNPs is described in our previous work (Pinna et al.).[33] The properties of the particles synthesized here are described in Table 1. The primary

Table 1. Properties of the MSNPs

Hydrodynamic diameter (nm) from DLS (in water, pH 6.4)	90.72 ± 11.91 nm, PDI 0.62
Primary diameter (from TEM) for n = 50 particles	d = 80 ± 11 nm
Zeta potential (meV)	−31.39 ± 0.42 mV
Surface area (m²/g)	724.88 ± 18.05 m²/g
Pore volume (cm³/g)	1.05 ± 0.01 cm³/g
Pore diameter (nm)	2.83 ± 0.07 nm

diameter distribution of the MSNPs measured by TEM is shown in Supplementary Figure SI1. The high PDI of the particles (0.62) indicates a tendency of the particles to agglomerate in water. FTIR analysis showed a well-defined absorption peak for MSNPs at ~1100 cm⁻¹ with a relatively low absorption at 1300−1700 cm⁻¹ (Figure 1c). Accordingly, s-SNOM imaging of MSNPs yielded high contrast at 1100 cm⁻¹, with absorption arising from Si−O−Si asymmetric stretching vibrations.[34,35] At 1300 cm⁻¹ There is almost no contrast between the MSNPs and the mica substrate due to the absence of strong vibrational modes at this wavelength (Figure 1d, e).

Imaging Whole U-87 Malignant Glioma Cells with s-SNOM

Figure 2a shows the topography of the periphery of a U-87 MG cell and reveals a thin (~100 nm thick), sheet-like region, which is identified as the lamellipodium.[36] There are also finger-like structures that originate inside the lamellipodium and protrude outward from it, which are identified as filopodia.[37] Figure 2c is an image of the same cell region obtained with the 20x optical microscope built into the s-SNOM system and cropped to show only the region of interest. For reference, the whole image (which shows the whole cell) can be seen in Supplementary Figure SI2.

Figure 2b is an s-SNOM image of the same region of the cell acquired at a 1667 cm⁻¹ wavelength that corresponds to absorption of the amide moieties in proteins. The filopodia appeared darker than the rest of the cell, most likely because they contain actin filaments that are bundled together by actin-bundling proteins.[38]

It is important to note, however, that the increased s-SNOM signal could also be related to the topography since a change in sample thickness can affect the s-SNOM signal. Indeed, when the phase, ϕ_3, is plot against the cell height, Z, for each pixel (Figure 2d), the two are strongly correlated. Thus, the s-SNOM image in Figure 2b is dependent on the cell topography and not just the chemistry.
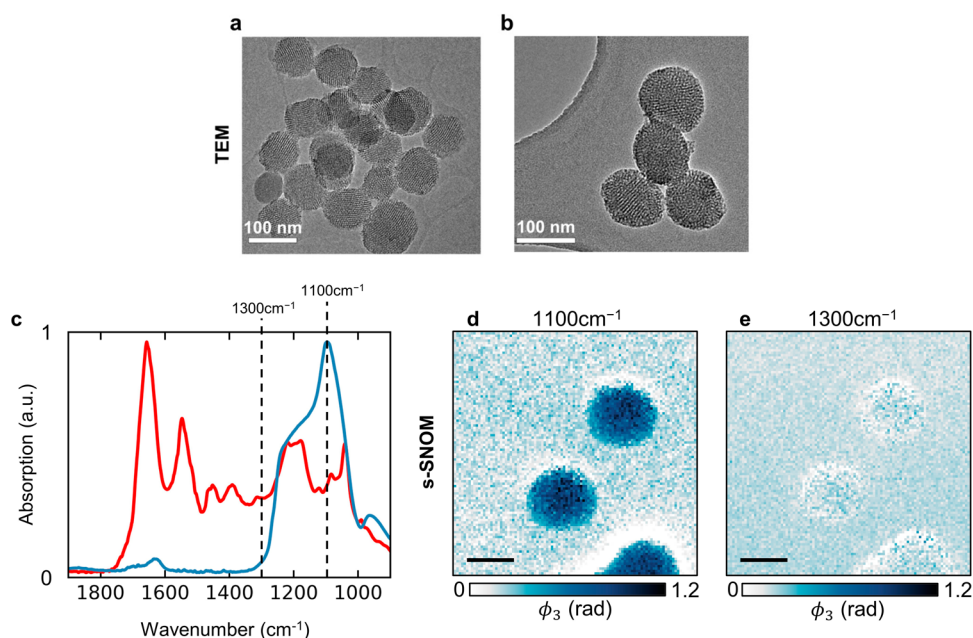
Figure 1. s-SNOM imaging of mesoporous silica nanoparticles (MSNPs). (a, b) TEM images of MSNPs. (c) FTIR absorption spectra of MSNPs (blue curve) and untreated U-87 MG cells (red curve). (d, e) s-SNOM images of MSNPs on a mica substrate acquired at 1100 and 1300 cm^{-1}, respectively. Scale bars 100 nm.
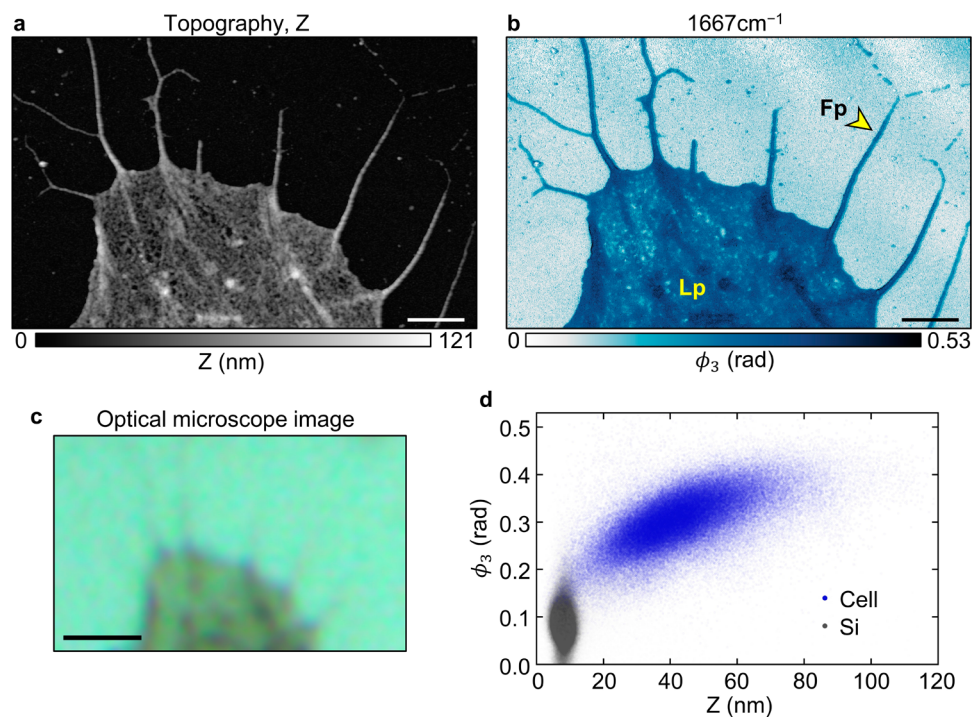

Figure 2. s-SNOM imaging of U-87 MG cells. (a) AFM topography of a region at the periphery of a U-87 MG cell. (b) s-SNOM image of the same region acquired at an imaging wavelength of 1667 cm^{-1}. (c) Corresponding region imaged with the built-in microscope in the s-SNOM system (cropped from the full image shown in Supplementary Figure SI2). (d) Correlation between the s-SNOM phase and the sample height was obtained using the values at each pixel in the images. The cell and the substrate were split into groups by masking images. Fp, filopodia; Lp, lamellipodium. Scale bars 2 μm (a, b), 5 μm (c).

We tested whether s-SNOM could detect MSNPs in air-dried U-87 human glioma cell preparations. As expected, s-SNOM phase images of U-87 allowed visualization of lamellipodia and filopodia at the nanoscale (Figure 3a, enlarged in Figure 3c), with cellular topography, e.g. the heights of the filopodia being provided by AFM. Tuning to

1100 cm^{-1}, the MSNPs were clearly seen, interacting with the cell or bound to the substrate, while they were absent in the 1300 cm^{-1} images (Figure 3c, insets i−iv).

On their own, the AFM topography images could be used to identify the MSNPs bound to the substrate (Figure 3b, 3c (i) but not all of those interacting with the cell membrane (Figure
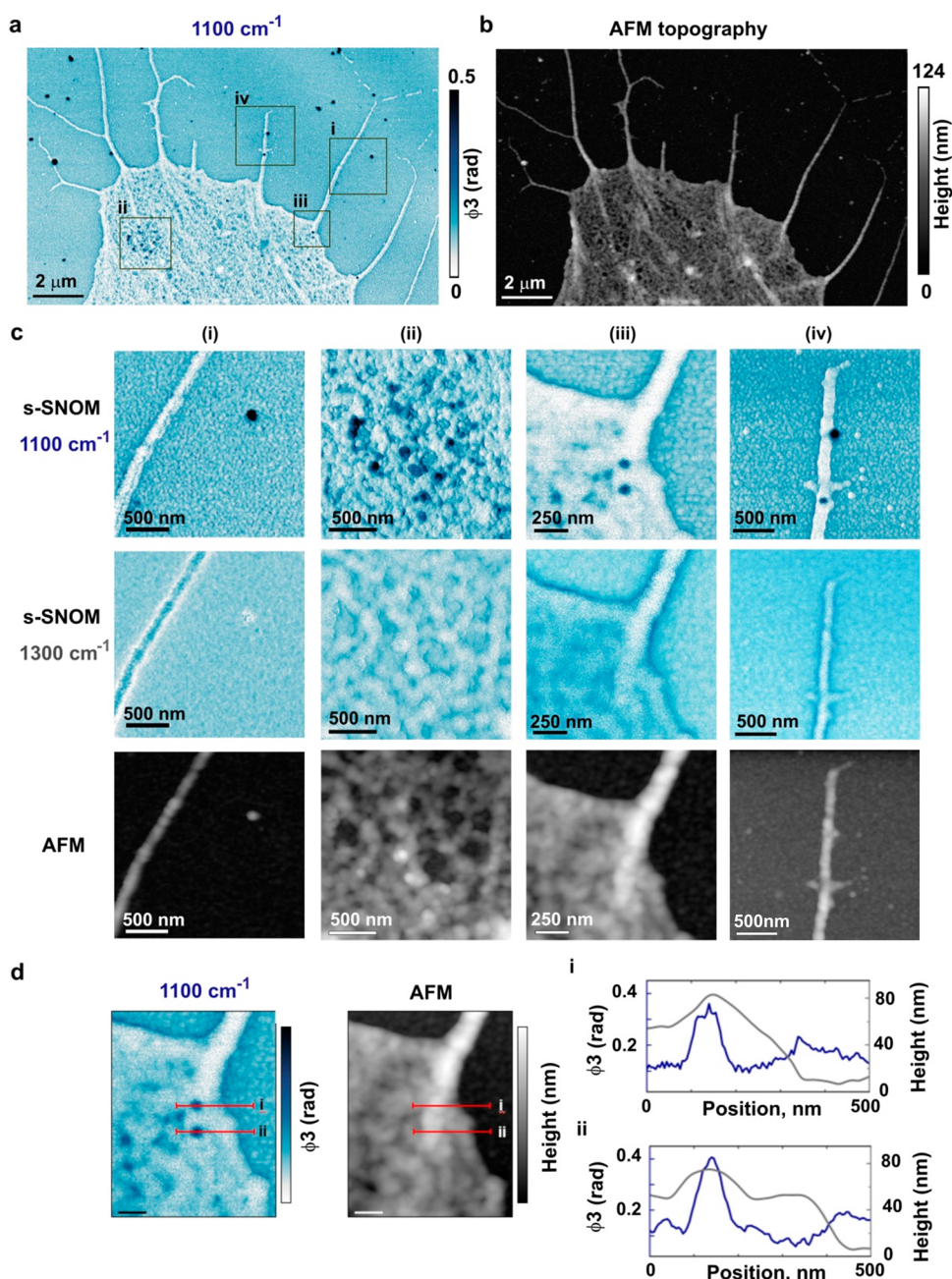
Figure 3. s-SNOM imaging of mesoporous silica nanoparticles (MSNPs) in U-87 MG cells. (a, b) s-SNOM (a, 1100 cm^{-1}) and AFM (b) images of an MSNP-treated air-dried U-87 MG cell. (c) Insets (i−iv), MSNP interaction with lamellopodia and filopodia, enlarged from (a), acquired at 1100 or 1300 cm^{-1}, and AFM images of the same regions.

3c, ii, (iii). Reliably detecting the MSNPs associated with or embedded into cell membranes (Figure 3c ii-iv) was only possible using the chemical sensitivity of s-SNOM.

Importantly, however, AFM images provide topographical mapping of the MSNP − cell interaction to supplement the chemical identification of MSNPs. Figure 4a−d shows high resolution s-SNOM and AFM images of MSNPs interacting with the U-87 MG cell shown in Figure 3. Line profiles of the s-SNOM phase and AFM topography across three MSNPs are shown in Figure 4e (i−iii) together with circles of d ∼ 80 nm (representing the MSNPs) as visual aids. The topography profile shown in Figure 4e, i follows a curvature that is consistent with the MSNP diameter, and its protrusion from the cell surface is only approximately 40 nm, which suggests

that the MSNP is only halfway (that is, partially) embedded into the cell. We note that the size of the MSNP estimated from the s-SNOM phase profile appears larger than 80 nm. This is consistent with the apparent size of MSNPs in Figure 3d. We expect that the surface of the MSNPs being exposed leads to a topographical effect on the s-SNOM signal.[39]

By contrast, the topography profiles in Figure 4e, ii and iii do not follow the curvature of the MSNPs. This might suggest that the MSNPs are fully embedded and internalized into the cell (that is, they are covered by the cell membrane). Thus, the complementary chemical and topographical mapping seemingly offers a means of distinguishing partially embedded MSNPs from those that are internalized, which is of huge importance for evaluating the efficacy of nanomedicines.
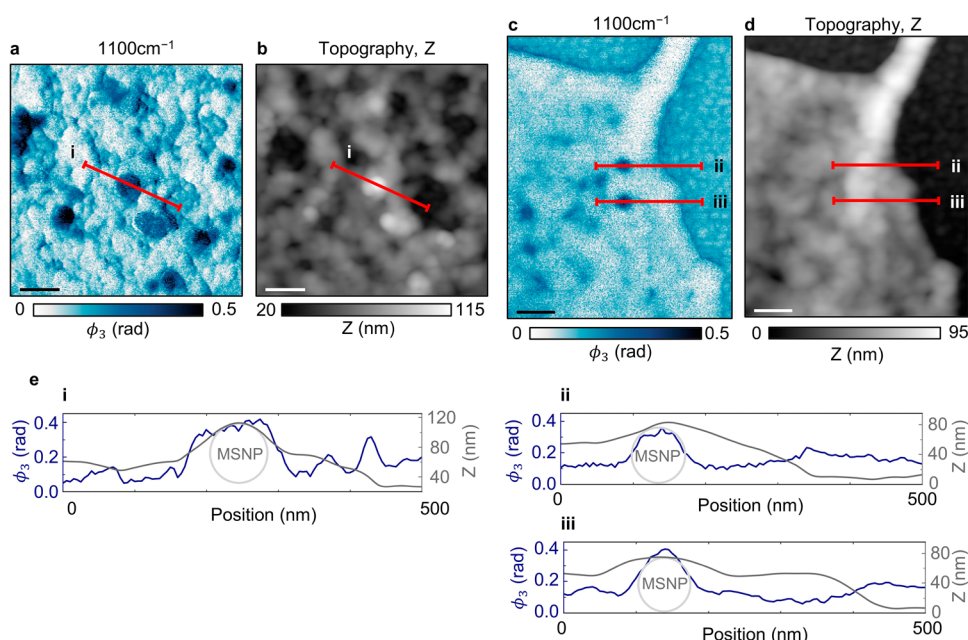
Figure 4. Correlating phase and topography profiles of mesoporous silica nanoparticles (MSNPs) in U-87 MG cells. (a−d) s-SNOM (a, c; 1100 cm^{-1}) and AFM (b, d) images of an MSNP-treated air-dried U-87 MG cell. (e) s-SNOM phase and topography profiles of three MSNPs interacting with the U-87 MG cell. MSNPs (spheres of d ∼ 80 nm) are shown for reference. Scale bars 200 nm.

We note that the MSNPs were mapped without modification and without using stains and/or labels. The stains needed for fluorescence microscopy could potentially disrupt cellular function and biochemistry in a way that could alter the interaction between the MSNPs and cells, and the fluorescence images would contain no information about the embedding status.

■ CONCLUSION

We have performed a preliminary study to demonstrate the potential of s-SNOM as a tool for imaging interactions of nanostructures through the depth of whole cells. We find that this approach allows us to visualize the spatial distribution of MSNPs both within and on the surface of GBM cells and eliminates the requirement of labeling either the particles or the cells.

The U-87 MG cells were imaged whole using a simple sample preparation technique, allowing the morphology of lamellipodia and filopodia to be seen, and the destinations of the MSNP within and bound to the cell to be found. This topographic information about the distribution of nanoparticles within cells is challenging to obtain by using other nanoscale 3D imaging techniques such as electron tomography.

Due to their attractive properties such as biocompatibility, high surface area for drug loading and biodegradability, MSNPs are being designed for several biomedical applications such as drug delivery vehicles to treat glioblastoma.[40] The advantages offered by s-SNOM could be beneficial for future understanding of the cell-based mechanisms by which MSNPs are internalized by cells, degrade/interact with subcellular organelles, and release their drug cargoes.

Here we have focused our efforts on imaging the ∼100 nm thick peripheries of U-87 MG cells, given their biological relevance for studying cancer invasiveness. The maximum depth at which MSNPs can be imaged inside cells remains to be determined. It has been shown that materials can be identified by their absorption signatures >100 nm below a sample surface.[28] It can therefore be expected that the MSNPs can be detected at this depth, especially given the large mid-IR contrast that is available between the MSNPs and the cell material. To formally test how deep inside cells s-SNOM can be used to detect MSNPs, it might in future be used in conjunction with a nanoscale 3D imaging technique such as a focused ion beam/scanning electron microscope (FIB/SEM) slice and view method (e.g., described in Guehrs et al.[41]). Alternatively, if the MSNPs are fluorescently labeled, 3D super-resolution microscopy might be used.

Future research may involve integrating these techniques with complementary methods such as mechanical AFM measurements of the stiffness of the cancer cells compared to healthy cells as another diagnostic marker.[42] This could be experimentally realized with the current s-SNOM setup by exchanging the s-SNOM probe for an AFM probe optimized for measuring cell stiffness.

s-SNOM might also be combined with fluorescence microscopy to provide rapid whole-cell imaging in addition to the nanoscale imaging demonstrated here. Correlative s-SNOM and confocal laser scanning microscopy has already been demonstrated,[43] as well as the imaging of fluorophore-coated nanoparticles,[44] which would be required for the confocal imaging. A valuable piece of future work would be to image fluorescently labeled MSNPs using s-SNOM so that s-SNOM images can be correlated with CLSM images.

Other bio applications in which chemical mapping of cells in 3D could reveal structures of interest include the imaging of amyloid beta sheets in primary neurons or the distribution specific IR sensitive drugs within intracellular organelles. To our knowledge, this is the first time that s-SNOM has been used for this purpose, and given the relative ease of sample preparation, we believe it could find a future role for the study of the efficacy of a wide range of therapeutic nanostructures.

■ MATERIALS AND METHODS

Mesoporous Silica Nanoparticle (MSNP) Synthesis

MSNP synthesis was performed using a modified sol−gel Stöber method.[45] Briefly, a solution of a precursor ("sol") is transformed through hydrolysis and condensation reaction into a gel, from which the solid part is isolated through centrifugation. The MSNPs are made mesoporous (pore diameters between 2 and 50 nm) by letting the nanoparticle structures grow around near-spherical surfactant aggregates (micelles) which are later removed, leaving voids (pores).[46]

The process for producing MSNPs was as follows (adapted from Pinna et al.[33]). The surfactant-based template for producing pores was prepared by adding 1 g of cetyltrimethylammonium bromide (CTAB) to 500 mL of distilled water. The pore template, contained in a flask, was immersed in paraffin oil at 70 °C and stirred at 600 rpm using a magnetic hot plate stirrer, followed by the addition of 3 mL of 2 M sodium hydroxide (NaOH) catalyst. A 5 mL portion of the silica-based precursor, tetraethyl orthosilicate (TEOS), was added to the pore template solution, followed by 5 mL of ethyl acetate (EtOAc). The solution was aged at 70 °C for 1 h with stirring (600 rpm) and 3 h without stirring to allow formation of nanoparticles. The solution was then centrifuged, and the pellet (of the nanoparticles) was washed three times in ethanol by centrifugation at 7830 rpm for 40 min (for each wash). Nanoparticles were isolated by drying the solution overnight at 60 °C. The CTAB surfactant was eliminated by thermal treatment at 550 °C-3 °C/min for 6 h, leaving voids (pores) in the nanoparticles.

The morphology and primary diameter distribution of the MSNPs were measured using TEM and ImageJ. The hydrodynamic diameter distribution of the MSNPs in water was measured using DLS for n = 3 repeats.

To confirm the size and morphology of MSNPs, the samples were imaged on 400 mesh copper grids coated with carbon film using bright-field TEM on the 200 kV 2100Plus. Different areas of the grid were analyzed by using ImageJ and the diameter of 50 nanoparticles from each sample were measured to calculate the mean size. The size distribution and zeta potential of the MSNPs were investigated using dynamic light scattering (DLS) and a ZetaSizer Nano ZS Malvern Instrument.

Cetyltrimethylammonium bromide (CTAB ≥ 98%, Sigma-Aldrich), sodium hydroxide (NaOH 2 M, Merck KGaA), tetraethyl orthosilicate (TEOS 99%, ABCR GmbH), and ethyl acetate (EtOAc 99.5%) were supplied by Acros Organics, ethanol (EtOH 99.9%) was supplied by VWR chemicals, and distilled water was used, as received, without any further purification.

U-87 MG Preparation and Treatment with MSNPs

U-87 MG human GBM cells, certified by the European Collection of Authenticated Cell Cultures, were supplied by Sigma-Aldrich. The cells were shipped on dry ice and stored at −140 °C in a nitrogen vapor freezer upon receipt. The frozen stocks were rapidly thawed using a temperature-controlled water bath set to 37 °C, and the cells were added to prewarmed complete culture medium Dulbecco's modified Eagle Medium (DMEM) supplemented with 10% Fetal Bovine Serum (FBS) and 1% penicillin/streptomycin) in a 15 mL falcon tube.

DMEM (+1 g/L D-glucose, L-glutamine, and pyruvate) (DMEM), FBS, and penicillin/streptomycin were supplied by

Gibco. The cells were pelleted by centrifugation at 130g for 7 min, excess medium was removed to ensure removal of dimethyl sulfoxide (DMSO) in the cryopreservation medium, and the cells were resuspended in a final volume of 10 mL complete culture medium.

The cells were then plated in tissue-culture-treated filter cap T75 flasks (Nunclon Delta). The cells were subcultured in a 1:4−1:5 ratio every 3−5 days, washing with DPBS and then using 0.25% Trypsin-EDTA to detach the cells from the plate. Dulbecco's phosphate-buffered saline (pH 7.0−7.3) (no calcium, no magnesium) was supplied by Gibco and the Trypsin Ethylenediaminetetraacetic acid (EDTA) was supplied by Sigma-Aldrich.

An aliquot of the low passage cells was retained and cryopreserved at $1-3 \times 10^6$ cells/mL in DMEM supplemented to final concentrations of 10% FBS and 5% DMSO by freezing slowly to −80 °C in a Nalgene M_r Frosty freezing container before transferring the cells to −140 °C for long-term storage. DMSO was supplied by Sigma-Aldrich.

Before freezing, healthy cells were quantified using 0.4% Trypan blue staining using a hemocytometer. The cells were discarded after 20 passages and replaced with cells from cryopreserved stocks. The received cells were certified free of mycoplasma, and the cells were routinely checked for fungal and bacterial contamination.

Samples were prepared by growing cells directly on 5 × 5 mm poly-L-lysine coated boron-doped ultraflat silicon wafer chips (NanoAndMore), prepared by incubating the UV-sterilized wafers in 0.01% poly-L-lysine solution (Sigma-Aldrich, UK) before allowing the wafers to air-dry under a laminar flow biosafety hood. The wafers were placed in 12-well microplates prior to cell seeding. Cells were incubated with 50 μg/mL of MSNPs for 24 h. In our previous work we confirmed, by acquiring TEM images of cell sections through the cells (shown in Supplementary Figure SI3), that MSNPs are internalized by a different cancerous cell line (MCF-7) at the same 24 h time point used here.[47] Following cell growth and treatment, the samples were rinsed in 0.1 M HEPES pH 7.2 and cells were fixed with 2.5% glutaraldehyde and 2.5% paraformaldehyde in 0.1 M HEPES for 30 min at room temperature. Fixatives were removed and cells were rinsed three times in 0.1 M (4-(2-hydroxyethyl)-1-piperazineethanesulfonic acid) (HEPES) buffer. Cells were dehydrated in a series of graded ethanol (EtOH) (12.5%, 25%, 50% and 70% for 5 min each, 95% and 100% for 2 × 5 min each). Cells were further dehydrated in hexamethyldisilazane (HMDS) (HMDS:EtOH 1:1 for 10 min, HMDS 2 × 10 min). HMDS was removed and cells were left to air-dry in a desiccator at room temperature.

s-SNOM Imaging of MSNP-Treated U-87 MG Cells

s-SNOM imaging was performed using a tapping amplitude of ∼50 nm. The cell height is typically much greater than the ∼3 μm travel range of the piezoelectric sample stage on the s-SNOM system, and therefore, it was not possible to capture a whole cell in one image. Imaging was instead focused on the lamellipodia and filopodia at the peripheries of the cells. These regions were chosen since, as discussed, they are the focus of many research questions related to cell movement, cancer migration and cell−cell transfer.[11,12,48]

No unexpected or unusually high safety hazards were encountered in any of the experimental methods used.

■ ASSOCIATED CONTENT

ⓈⒾ Supporting Information

The Supporting Information is available free of charge at https://pubs.acs.org/doi/10.1021/cbmi.4c00053.

Distribution of MSNP diameters as measured by TEM, 20× optical microscope image of U-87 MG cells, TEM images of MSNPs internalized by MCF-7 cancer cells after 24 h (PDF)

■ AUTHOR INFORMATION

Corresponding Authors

George E. Greaves − *Experimental Solid State Physics Group, Department of Physics, Imperial College, SW72AZ London, U.K.;* ⓞ orcid.org/0000-0002-5070-698X; Email: george.greaves15@imperial.ac.uk

Chris C. Phillips − *Experimental Solid State Physics Group, Department of Physics, Imperial College, SW72AZ London, U.K.;* Email: chris.phillips@imperial.ac.uk

Authors

Alessandra Pinna − *Department of Materials and London Centre for Nanotechnology, Imperial College, SW72AZ London, U.K.; School of Veterinary Medicine, Faculty of Health and Medical Sciences, University of Surrey, Guildford GU2 7XH, U.K.; The Francis Crick Institute, NW1 1AT London, U.K.;* ⓞ orcid.org/0009-0001-4467-8484

Jonathan M. Taylor − *Department of Materials and London Centre for Nanotechnology, Imperial College, SW72AZ London, U.K.*

Alexandra E. Porter − *Department of Materials and London Centre for Nanotechnology, Imperial College, SW72AZ London, U.K.*

Complete contact information is available at:
https://pubs.acs.org/10.1021/cbmi.4c00053

Author Contributions

The project was conceived and coordinated by C.C.P. and A.E.P. MSNPs were produced by A.P. The procedure for growing malignant glioma cells, incubating them with MSNPs, and preparing them for s-SNOM imaging was developed by J.M.T. The authors thank Darya Kiryushko for producing the cells used in this study in accordance with J.M.T's procedure. s-SNOM and AFM images were acquired and analyzed by G.E.G. Infrared absorption spectra were acquired by G.E.G. The manuscript was written by G.E.G., A.E.P., and C.C.P. and has been read, contributed to, and acknowledged by all authors.

Notes

The authors declare no competing financial interest.

■ ACKNOWLEDGMENTS

■ REFERENCES

(1) Ocelic, N.; Huber, A.; Hillenbrand, R. Pseudoheterodyne detection for background-free near-field spectroscopy. *Appl. Phys. Lett.* **2006**, *89*, 101124.

(2) Mester, L.; Govyadinov, A. A.; Hillenbrand, R. High-fidelity nano-FTIR spectroscopy by on-pixel normalization of signal harmonics. *Nanophotonics* **2022**, *11*, 377−390.

(3) Huth, F.; Govyadinov, A.; Amarie, S.; Nuansing, W.; Keilmann, F.; Hillenbrand, R. Nano-FTIR Absorption Spectroscopy of Molecular Fingerprints at 20 nm Spatial Resolution. *Nano Lett.* **2012**, *12*, 3973−3978.

(4) Keilmann, F.; Amarie, S. Mid-infrared frequency comb spanning an octave based on an Er fiber laser and difference-frequency generation. *Journal of Infrared, Millimeter, and Terahertz Waves* **2012**, *33*, 479−484.

(5) Amarie, S.; Ganz, T.; Keilmann, F. Mid-infrared near-field spectroscopy. *Opt. Express* **2009**, *17*, 21794−21801.

(6) Huth, F.; Schnell, M.; Wittborn, J.; Ocelic, N.; Hillenbrand, R. Infrared-spectroscopic nanoimaging with a thermal source. *Nature materials* **2011**, *10*, 352−356.

(7) Xiao, L.; Schultz, Z. D. Spectroscopic imaging at the nanoscale: Technologies and recent applications. *Analytical chemistry* **2018**, *90*, 440.

(8) Raschke, M. B.; Lienau, C. Apertureless near-field optical microscopy: Tip-sample coupling in elastic light scattering. *Appl. Phys. Lett.* **2003**, *83*, 5089−5091.

(9) Keilmann, F.; Hillenbrand, R. Near-field microscopy by elastic light scattering from a tip. *Philosophical Transactions of the Royal Society of London. Series A: Mathematical, Physical and Engineering Sciences* **2004**, *362*, 787−805.

(10) Atkin, J. M.; Berweger, S.; Jones, A. C.; Raschke, M. B. Nano-optical imaging and spectroscopy of order, phases, and domains in complex solids. *Adv. Phys.* **2012**, *61*, 745−842.

(11) Cheng, W.-Y.; Chiao, M.-T.; Liang, Y.-J.; Yang, Y.-C.; Shen, C.-C.; Yang, C.-Y. Luteolin inhibits migration of human glioblastoma U-87 MG and T98G cells through downregulation of Cdc42 expression and PI3K/AKT activity. *Molecular biology reports* **2013**, *40*, 5315−5326.

(12) Civita, P.; Leite, D. M.; Pilkington, G. J. Pre-clinical drug testing in 2D and 3D human in vitro models of glioblastoma incorporating non-neoplastic astrocytes: tunneling nano tubules and mitochondrial transfer modulates cell behavior and therapeutic response. *International Journal of Molecular Sciences* **2019**, *20*, 6017.

(13) Yamaguchi, H.; Condeelis, J. Regulation of the actin cytoskeleton in cancer cell migration and invasion. *Biochimica et Biophysica Acta (BBA)-Molecular Cell Research* **2007**, *1773*, 642−652.

(14) Greaves, G.; Allison, L.; Machado, P.; Morfill, C.; Fleck, R.; Porter, A. E.; Phillips, C. Infrared nanoimaging of neuronal ultrastructure and nanoparticle interaction with cells. *Nanoscale* **2024**, *16*, 6190.

(15) Greaves, G. E.; Kiryushko, D.; Auner, H. W.; Porter, A. E.; Phillips, C. C. Label-free nanoscale mapping of intracellular organelle chemistry. *Communications Biology* **2023**, *6*, 583.

(16) Mastel, S.; Govyadinov, A. A.; Maissen, C.; Chuvilin, A.; Berger, A.; Hillenbrand, R. Understanding the Image Contrast of Material Boundaries in IR Nanoscopy Reaching 5 nm Spatial Resolution. *ACS Photonics* **2018**, *5*, 3372−3378.

(17) Paidi, S. K.; Troncoso, J. R.; Harper, M. G.; Liu, Z.; Nguyen, K. G.; Ravindranathan, S.; Rebello, L.; Lee, D. E.; Ivers, J. D.; Zaharoff, D. A.; et al. Raman spectroscopy reveals phenotype switches in breast cancer metastasis. *Theranostics* **2022**, *12*, 5351.

(18) Short, M. A.; Lam, S.; McWilliams, A.; Zhao, J.; Lui, H.; Zeng, H. Development and preliminary results of an endoscopic Raman probe for potential in vivo diagnosis of lung cancers. *Opt. Lett.* **2008**, *33*, 711−713.

(19) Lui, H.; Zhao, J.; McLean, D.; Zeng, H. Real-time Raman spectroscopy for in vivo skin cancer diagnosis. *Cancer research* **2012**, *72*, 2491−2500.

(20) Potcoava, M. C.; Futia, G. L.; Aughenbaugh, J.; Schlaepfer, I. R.; Gibson, E. A. Raman and coherent anti-Stokes Raman scattering microscopy studies of changes in lipid content and composition in hormone-treated breast and prostate cancer cells. *Journal of Biomedical Optics* **2014**, *19*, 111605−111605.

(21) Kurouski, D.; Dazzi, A.; Zenobi, R.; Centrone, A. Infrared and Raman chemical imaging and spectroscopy at the nanoscale. *Chem. Soc. Rev.* **2020**, *49*, 3315−3347.

(22) Kusch, P.; Mastel, S.; Mueller, N. S.; Morquillas Azpiazu, N.; Heeg, S.; Gorbachev, R.; Schedin, F.; Hubner, U.; Pascual, J. I.; Reich, S.; et al. Dual-scattering near-field microscope for correlative nanoimaging of SERS and electromagnetic hotspots. *Nano Lett.* **2017**, *17*, 2667−2673.

(23) Freitas, R. O.; Cernescu, A.; Engdahl, A.; Paulus, A.; Levandoski, J. E.; Martinsson, I.; Hebisch, E.; Sandt, C.; Gouras, G. K.; Prinz, C. N.; Deierborg, T.; Borondics, F.; Klementieva, O. Nano-Infrared Imaging of Primary Neurons. *Cells* **2021**, *10*, 2559.

(24) Tranca, D. E.; Stanciu, S. G.; Hristu, R.; Witgen, B. M.; Stanciu, G. A. Nanoscale mapping of refractive index by using scattering-type scanning near-field optical microscopy. *Nanomedicine: Nanotechnology, Biology and Medicine* **2018**, *14*, 47−50.

(25) Zhang, W.; Chen, Y. Visibility of subsurface nanostructures in scattering-type scanning near-field optical microscopy imaging. *Opt. Express* **2020**, *28*, 6696−6707.

(26) Kusnetz, B.; Belhassen, J.; Tranca, D. E.; Stanciu, S. G.; Anton, S.-R.; Zalevsky, Z.; Stanciu, G. A.; Karsenty, A. Generic arrays of surface-positioned and shallow-buried gold multi-shapes as reference samples to benchmark near-field microscopes. Part 1: Applications in s-SNOM depth imaging. *Results in Physics* **2024**, *56*, 107318.

(27) Stanciu, S. G.; Tranca, D. E.; Zampini, G.; Hristu, R.; Stanciu, G. A.; Chen, X.; Liu, M.; Stenmark, H. A.; Latterini, L. Scattering-type scanning near-field optical microscopy of polymer-coated gold nanoparticles. *ACS omega* **2022**, *7*, 11353−11362.

(28) Mester, L.; Govyadinov, A. A.; Chen, S.; Goikoetxea, M.; Hillenbrand, R.; et al. Subsurface chemical nanoidentification by nano-FTIR spectroscopy. *Nat. Commun.* **2020**, *11*, 3359.

(29) Vivero-Escoto, J. L.; Slowing, I. I.; Trewyn, B. G.; Lin, V. S. Y. Mesoporous silica nanoparticles for intracellular controlled drug delivery. *Small* **2010**, *6*, 1952−1967.

(30) Zhou, Y.; Quan, G.; Wu, Q.; Zhang, X.; Niu, B.; Wu, B.; Huang, Y.; Pan, X.; Wu, C. Mesoporous silica nanoparticles for drug and gene delivery. *Acta Pharm. Sin B* **2018**, *8*, 165−177.

(31) Szekeres, M.; Tóth, J.; Dékány, I. Specific surface area of stoeber silica determined by various experimental methods. *Langmuir* **2002**, *18*, 2678−2685.

(32) Ritter, H.; Ramm, J. H.; Brühwiler, D. Influence of the Structural Properties of Mesoporous Silica on the Adsorption of Guest Molecules. *Materials (Basel)* **2010**, *3*, 4500−4509.

(33) Pinna, A.; Torki Baghbaderani, M.; Vigil Hernández, V.; Naruphontjirakul, P.; Li, S.; McFarlane, T.; Hachim, D.; Stevens, M. M.; Porter, A. E.; Jones, J. R. Nanoceria provides antioxidant and osteogenic properties to mesoporous silica nanoparticles for osteoporosis treatment. *Acta Biomaterialia* **2021**, *122*, 365−376.

(34) Liu, F.; Wang, J.; Huang, P.; Zhang, Q.; Deng, J.; Cao, Q.; Jia, J.; Cheng, J.; Fang, Y.; Deng, D. Y.; et al. Outside-in stepwise functionalization of mesoporous silica nanocarriers for matrix type sustained release of fluoroquinolone drugs. *J. Mater. Chem. B* **2015**, *3*, 2206−2214.

(35) Mehmood, Y.; Khan, I. U.; Shahzad, Y.; Khalid, S. H.; Asghar, S.; Irfan, M.; Asif, M.; Khalid, I.; Yousaf, A. M.; Hussain, T. Facile synthesis of mesoporous silica nanoparticles using modified sol-gel method: Optimization and in vitro cytotoxicity studies. *Pak. J. Pharm. Sci.* **2019**, *32*, 1805−1812.

(36) Small, J. V.; Stradal, T.; Vignal, E.; Rottner, K. The lamellipodium: where motility begins. *Trends in Cell Biology* **2002**, *12*, 112−120.

(37) Mattila, P. K.; Lappalainen, P. Filopodia: molecular architecture and cellular functions. *Nat. Rev. Mol. Cell Biol.* **2008**, *9*, 446−454.

(38) Khurana, S.; George, S. P. The role of actin bundling proteins in the assembly of filopodia in epithelial cells. *Cell Adhesion & Migration* **2011**, *5*, 409−420.

(39) Chen, X.; Yao, Z.; Stanciu, S. G.; Basov, D.; Hillenbrand, R.; Liu, M. Rapid simulations of hyperspectral near-field images of three-dimensional heterogeneous surfaces. *Opt. Express* **2021**, *29*, 39648−39668.

(40) Janjua, T. I.; Cao, Y.; Ahmed-Cox, A.; Raza, A.; Moniruzzaman, M.; Akhter, D. T.; Fletcher, N. L.; Kavallaris, M.; Thurecht, K. J.; Popat, A. Efficient delivery of Temozolomide using ultrasmall large-pore silica nanoparticles for glioblastoma. *J. Controlled Release* **2023**, *357*, 161−174.

(41) Guehrs, E.; Schneider, M.; Günther, C. M.; Hessing, P.; Heitz, K.; Wittke, D.; López-Serrano Oliver, A.; Jakubowski, N.; Plendl, J.; Eisebitt, S.; et al. Quantification of silver nanoparticle uptake and distribution within individual human macrophages by FIB/SEM slice and view. *J. Nanobiotechnol.* **2017**, *15*, 1−11.

(42) Huml, M.; Silye, R.; Zauner, G.; Hutterer, S.; Schilcher, K. Brain tumor classification using AFM in combination with data mining techniques. *BioMed. research international* **2013**, *2013*, 176519.

(43) Stanciu, S. G.; Tranca, D. E.; Hristu, R.; Stanciu, G. A. Correlative imaging of biological tissues with apertureless scanning near-field optical microscopy and confocal laser scanning microscopy. *Biomed. Opt. Express* **2017**, *8*, 5374−5383.

(44) Tranca, D. E.; Stanciu, S. G.; Hristu, R.; Latterini, L.; Stanciu, G. A. Surface optical characterization at nanoscale using phasor representation of data acquired by scattering scanning near-field optical microscopy. *Appl. Surf. Sci.* **2020**, *509*, 145347.

(45) Stöber, W.; Fink, A.; Bohn, E. Controlled growth of monodisperse silica spheres in the micron size range. *J. Colloid Interface Sci.* **1968**, *26*, 62−69.

(46) Grün, M.; Lauer, I.; Unger, K. K. The synthesis of micrometer- and submicrometer-size spheres of ordered mesoporous oxide MCM-41. *Adv. Mater.* **1997**, *9*, 254−257.

(47) Chen, S.; Greasley, S.; Ong, Z.; Naruphontjirakul, P.; Page, S.; Hanna, J.; Redpath, A.; Tsigkou, O.; Rankin, S.; Ryan, M.; et al. Biodegradable zinc-containing mesoporous silica nanoparticles for cancer therapy. *Materials Today Advances* **2020**, *6*, 100066.

(48) Jacquemet, G.; Hamidi, H.; Ivaska, J. Filopodia in cell adhesion, 3D migration and cancer cell invasion. *Curr. Opin. Cell Biol.* **2015**, *36*, 23−31.